Journal of Infrared, Millimeter, and Terahertz Waves (2026) 47:35
https://doi.org/10.1007/s10762-026-01141-4

RESEARCH

Design and Operational Strategies for Mitigating Static After Cavity Interaction Based on the European ITER Gyrotron

André Schmidt[1] · Konstantinos Avramidis[2] · Lukas Feuerstein[1] · Stefan Illy[1] · John Jelonnek[1] · Manfred Thumm[1] · Chuanren Wu[1]

Received: 27 February 2026 / Accepted: 26 April 2026 / Published online: 11 May 2026

Abstract
Gyrotrons are essential sources for electron cyclotron resonance heating in magnetic confinement fusion devices. Achieving high overall efficiency and the nominal design power in these devices is a critical requirement. However, discrepancies between theoretical models and experimental results often arise because real systems exhibit additional effects that are not fully captured in idealized simulations. One such effect is the static after-cavity interaction (ACI) of the same transverse electric (TE) mode in the cavity uptaper and quasi-optical launcher, which can significantly reduce performance. A thorough understanding of ACI, supported by advanced simulation tools, is essential to identify effective mitigation strategies. Practical measures include fine adjustments of the magnetic field, operation at alternative working points, or modifications to the launcher geometry. Such approaches offer promising potential to enhance overall efficiency in gyrotrons for present and future fusion applications.

Keywords Gyrotrons · After-cavity interaction · EU ITER gyrotron

1 Introduction

Gyrotrons serve as high-power RF sources for electron cyclotron resonance heating in magnetic confinement fusion devices such as ITER. Achieving the nominally designed output power with a consistently high overall efficiency is key to their design and operation. The total efficiency is determined by multiple factors, including interaction efficiency, collector performance, and losses in the quasi-optical transmission system.

The internal geometry of the gyrotron strongly affects these efficiency metrics. Directly after the interaction cavity, an uptaper connects the cavity to the launcher,

✉ André Schmidt
andre.schmidt@kit.edu

[1] Institute for Pulsed Power and Microwave Technology (IHM), Karlsruhe Institute of Technology (KIT), Karlsruhe, Germany

[2] Department of Physics, National and Kapodistrian University of Athens (NKUA), Athen, Greece

designed to gradually increase the waveguide radius minimizing mode conversion. The launcher transforms the cavity field into a Gaussian beam and couples it into the quasi-optical transmission system. The launcher entry is characterized by the oversize factor, defined as the increase of the wall radius relative to the cavity radius. Variations in the oversize factor alter the coupling between the electron beam and the electromagnetic wave within the uptaper and launcher, thereby affecting the occurrence and magnitude of static after-cavity interaction (ACI). Static ACI arises when the electron beam interacts with the same mode at the same frequency as in the cavity under the resonance condition at a reduced magnetic field. This interaction is detrimental because it returns energy from the RF field to the electrons, reducing interaction and collector efficiency. The mechanisms and impact of static ACI have been investigated in various studies, such as [1–3]. Dynamic ACI, defined as the interaction with the same mode at a different frequency, has been examined in previous studies [4–7] and is not considered in this work. In the following, the term ACI refers exclusively to static ACI. Other phenomena in this region, such as excitation of other modes, mode conversion in the launcher, and backward waves, have also been investigated in previous studies ([8, 9]) and are beyond the scope of the present study.

In the present work, several improvements are introduced in the simulation framework to more accurately capture and quantify ACI. These include the incorporation of voltage depression of the electron beam and variations in the operating point, allowing for a more realistic and controlled assessment of the phenomenon. Furthermore, particular emphasis is placed on the role of the launcher radius in connection to the operating point.

Comparisons with experimental data of gyrotrons have been reported in [10] and [11]. In the present work, the European (EU) ITER gyrotron [12] is taken as a representative example, for which ACI has not yet been investigated. The objective is to understand the mechanisms of ACI and to identify practical strategies for mitigating its effects, thereby improving interaction efficiency without requiring major modifications to existing gyrotron designs.

2 Fundamental Considerations

A common factor for the strength of the interaction between the TE electromagnetic wave and the electron beam is described by the coupling coefficient $G(z)$, as defined in [13]:

$$G(z) = \frac{J^2_{\mathrm{m}\pm s}\left(\frac{\chi\, r(z)}{R(z)}\right)}{\left(\chi^2 - \mathrm{m}^2\right) J^2_{\mathrm{m}}(\chi)} \text{ with } r(z) = r_{\min}\sqrt{\frac{B_{\max}}{B(z)}}. \tag{1}$$

Here, J denotes the Bessel function of the first kind, m is the azimuthal mode index, and s represents the cyclotron harmonic. The eigenvalue χ is defined as the n-th zero of the derivative of the Bessel function. The function $R(z)$ defines the wall radius, while the electron beam radius $r(z)$ varies along the axial direction due to magnetic compression. The minimum beam radius $r_{\min}$ occurs at the position of the maximum

magnetic field $B_{\max}$ in the cavity. The axial magnetic field profile $B(z)$ thus determines how the beam expands in the uptaper region.

The occurrence of ACI is determined by the resonance condition between the electron beam and the cavity output wave. For interaction to occur, the wave frequency must approximately match the electron cyclotron frequency corrected by the Doppler term, as expressed by the resonance condition:

$$\omega_{\text{wave}} \approx \omega_{\text{electron}} + \omega_{\text{doppler}}. \tag{2}$$

Here, ω_{wave} is the frequency of the electromagnetic wave produced in the cavity propagating into uptaper and launcher, and the right-hand side describes the electron frequency plus the Doppler frequency. The term for the electron beam is given by

$$\omega_{\text{electron}} = \frac{e}{m}\frac{B(z)}{\gamma(z)}, \tag{3}$$

where e and m are the elemental charge and electron mass and $\gamma(z)$ is the relativistic Lorentz factor of the electrons. The Doppler term accounts for the longitudinal motion of the electrons:

$$\omega_{\text{doppler}} = k_z(z)v_z(z), \tag{4}$$

with $k_z(z)$ the longitudinal wave number and $v_z(z) = c\beta_z(z)$ the mean axial velocity of the electrons. In the oversized launcher, the Doppler contribution becomes particularly significant due to the increased axial wavenumber of the field. Expressing $k_z(z)$ through the wave dispersion relation in the circular waveguide leads to

$$k_z(z) = \sqrt{k^2 - k_c^2}, \tag{5}$$

where $k = \frac{\omega_{\text{wave}}}{c}$ is the free-space wavenumber and $k_c = \frac{\chi}{R(z)}$ the cutoff wavenumber of the excited mode. Substituting yields the final form of the resonance condition:

$$\omega_{\text{wave}} \approx \frac{e}{m}\frac{B(z)}{\gamma(z)} + \beta_z(z)\sqrt{\omega_{\text{wave}}^2 - \left(c\frac{\chi}{R(z)}\right)^2}. \tag{6}$$

This relation shows explicitly how the fulfillment of the resonance condition depends on the axial magnetic field, the varying waveguide radius, and the electron beam dynamics along the z-direction. Unless stated otherwise, the description of the electron beam dynamics in the following is based on average values. These dependencies determine the axial locations where interaction can occur.

Using the Eqs. 1 and 6, the effect of ACI can be mitigated by positioning the resonance condition in regions where the coupling coefficient $G(z)$ is minimized.

3 Mitigation of ACI

This study examines three strategies for mitigating ACI. The first is to change the operating point, thereby shifting the resonance condition. The second is to adjust the launcher radius, which modifies the position of maximum coupling while only slightly affecting the Doppler term in the resonance condition. The third is to employ an alternative magnetic field profile, which can reduce the overall influence of ACI.

3.1 Influence of Operation Point

At straightforward approach to mitigate the influence of ACI is to adjust the operating point, which can be implemented in existing gyrotrons without requiring major design modifications. To identify an operating point that effectively reduces ACI, it is necessary to quantify how the ACI level depends on the chosen operating parameters. For that, the normalized magnetic field profile $B(z)/B_{\max}$ is used. As a first approximation, a constant launcher radius with an oversize factor of 1.07 is assumed. Since the coupling coefficient $G(z)$ scales with the ratio of the electron beam radius to the outer wall radius, the magnetic field, where the coupling equals that in the cavity, can be identified.

$$\frac{r_{\min}}{R_{\text{cav}}} \stackrel{!}{=} \frac{r(z)}{R_{\text{launcher}}} = \frac{r_{\min}\sqrt{\frac{B_{\max}}{B(z)}}}{1.07 \cdot R_{\text{cav}}} \tag{7}$$

$$\frac{B(z)}{B_{\max}} = \frac{1}{1.07^2} \approx 0.87 \tag{8}$$

This relative magnetic field strength should be avoided when fulfilling the resonance condition, as it leads to a strong interaction with ACI. To get the magnetic field at the fulfilled resonance condition, we apply a transformation of the resonance condition formula, as described in equation (6) of [1]:

$$\frac{B(z)}{B_{\max}} = \frac{1 - \beta_z(z)\sqrt{1 - \left(\frac{R_{\text{cav}}}{R_{\text{launcher}}}\right)^2}}{\left(1 - \frac{\Delta\omega}{\omega_{\text{wave}}}\right)\frac{\gamma_0}{\gamma}} \tag{9}$$

$$\text{with } \frac{\gamma_0}{\gamma} = \frac{1 + \frac{E_{\text{kin}}}{511\,\text{keV}}}{1 + \frac{E_{\text{kin}}}{511\,\text{keV}}(1 - \eta_{\text{int}})}. \tag{10}$$

For an initial estimation using realistic parameters, the example from [1] is adopted, with the exception of $R_{\text{launcher}} = 1.07\,R_{\text{cav}}$. With these parameters, the corresponding magnetic field ratio in the launcher would be approximately 0.87. Under these conditions, the resonance is fulfilled at the location where the electron beam couples most strongly to the wave, representing the most unfavorable scenario for ACI mitigation. To verify whether this behavior also occurs in the EU ITER gyrotron, an improved simulation, incorporating refined physical models, is performed.

Table 1 Operating parameters of the EU ITER gyrotron

Parameter	Value	Spread
$E_{\text{kin}}(z = 0\,\text{mm})$	79.5 kV	±0.74 %
$\alpha(z = 0\,\text{mm})$	1.25	±20 %
r_{min}	9.44 mm	±1 %
B_{max}	6.78 T	
Current I	40 A	
Beam neutralization	70 %	

3.1.1 EU ITER Gyrotron Case Study

As a representative case, the EU, $\text{TE}_{32,9}$, 170 GHz, 1 MW ITER gyrotron as described in [12] is with input parameters from Table 1 is considered. The spreads in kinetic energy and pitch factor α are evaluated at the entrance of the cavity and assumed to follow normal distributions with standard deviation σ and a considered range corresponding to $\pm 2\sigma$. The spread of the electron beam radius is assumed to be uniformly distributed within the specified range.

The cavity geometry, together with the magnetic field and adjusted magnetic fields for Sect. 3.3, are shown in Fig. 1. The origin refers to the beginning of the downtaper, the center of the cavity is located at $z = 36.5$ mm, and the launcher starts at $z = 107.5$ mm with an oversize factor of 1.07 and a tapering of 0.002.

The axial electron velocity $\beta_z(z)$ is affected by several factors (see equation (5) in [14]), including magnetic compression, voltage depression, and the RF field in the cavity. To account for these interdependent effects, the interaction is analyzed using a simulation rather than an analytical approach. The gyrotron model is implemented in the time-dependent self-consistent interaction code ROCK [14]. Based on the simulation results and Eqs. 1 and 6, the change of $f(z)$, $\gamma(z)$, and $G(z)$ along the z-axis is obtained, as illustrated in Fig. 2.

At the center of the cavity, the resonance condition is satisfied, as shown in Fig. 2, with f_{wave} intersecting $f_{\text{electron}} + f_{\text{doppler}}$. The cavity is specifically designed to maxi-

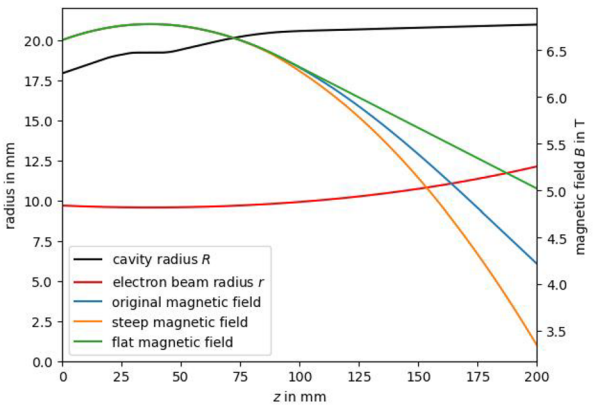

Fig. 1 Cavity geometry with 3 different magnetic field profiles along z and the electron beam trajectory corresponding to the original magnetic field

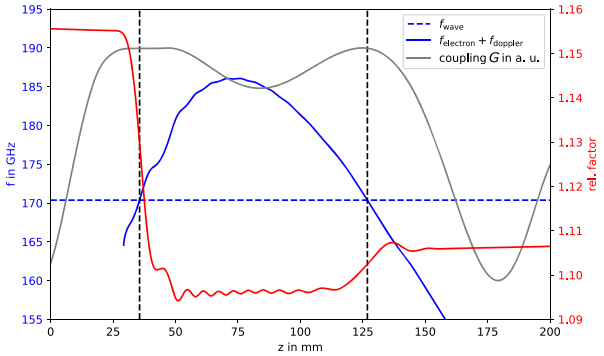

Fig. 2 Change of $f(z)$ (blue), $\gamma(z)$ (red), and $G(z)$ (gray) along the interaction region and into the launcher for an EU ITER gyrotron. Black dashed lines indicate positions along z where the resonance condition is satisfied

mize coupling between the electron beam and the RF field, resulting in highly efficient energy transfer from the electrons to the wave. This is reflected in the rapid decrease of the relativistic factor $\gamma(z)$ along the interaction region. Within the launcher, the resonance condition is again fulfilled at $z = 126.5\,\text{mm}$, providing another site for beam-wave interaction. As anticipated from the earlier estimation, the coupling coefficient $G(z)$ is near its maximum at this location, leading to strong ACI. Here, energy from the existing RF field is transferred back to the electrons, causing an increase in $\gamma(z)$.

This high ACI is detrimental, as it directly reduces the potential output power of the gyrotron and degrades overall efficiency. In the present case, the output power decreases by approximately 150 kW, corresponding to a reduction in interaction efficiency from 37.1 % to 33 %.

As illustrated in Fig. 3, electrons do not all gain or lose the same amount of energy during the interaction. The figure shows the trajectories of individual electrons, indicating whether they undergo acceleration or deceleration within the cavity and during

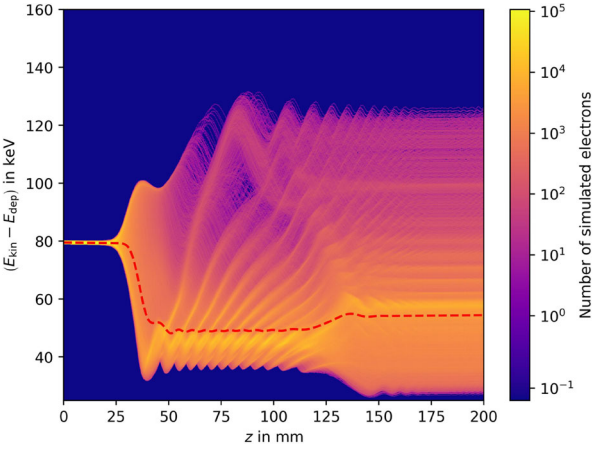

Fig. 3 Simulated electron distribution along z as a function of electron energy for the EU ITER gyrotron case. The red dashed line shows the average kinetic energy

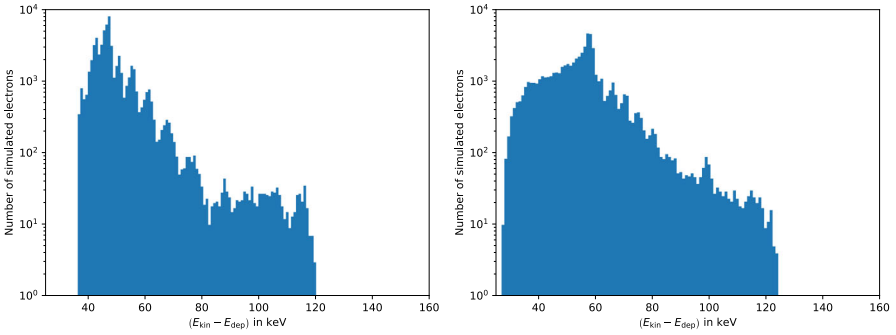

(a) z = 100 mm (b) z = 200 mm

Fig. 4 Electron distribution over the kinetic energy at different positions in the geometry

the subsequent ACI process. Notably, some of the slowest electrons are further decelerated. For a more precise comparison, the energy distributions at $z = 100$ mm and at $z = 200$ mm are shown in Fig. 4. The energy of the lowest 5 % of electrons decreases from 38.4 keV to 30.6 keV, which limits the voltage that can be applied to a depressed collector and therefore additionally reduces the overall efficiency [15]. For these reasons, minimizing the coupling in the region where the resonance condition is fulfilled is essential to reduce ACI. Achieving this reduction is the focus of the next section.

3.1.2 Effects of Operating Point Adjustment

To shift the location of maximum coupling away from the resonance condition, it is most effective to adjust β_z and/or E_{kin}, while minimizing the impact on the interaction within the cavity. Revisiting Eq. 9 shows that both lower- and higher-voltage operation are feasible, as either choice shifts the magnetic field away from the value corresponding to maximum coupling.

For operation at 60 kV, β_z changes to 0.3, and the magnetic field ratio at which the resonance condition is satisfied changes from 0.87 to 0.89. At 90 kV, β_z becomes 0.38, with $B/B_{\text{cav}} = 0.847$. Selecting an operating point based solely on β_z is challenging, due to its dependence on multiple factors; therefore, the simulations instead focus on increasing E_{kin}, as illustrated in Fig. 5.

In the figure, the blue curve represents the RF power at the launcher entrance at 107.5 mm, while the green and orange curves with difference in spreads show the output power at $z = 200$ mm. Fluctuations in these curves arise because variations in E_{kin} affect the parameters ω_{wave}, $\gamma(z)$, and $\beta_z(z)$ in Eq. 6, which in turn modulates the occurrence of ACI along the launcher and, consequently, its strength. Including electron beam spreads averages out these oscillations, as each electron experiences slightly different parameters, as reflected in the orange curve. For both cases, deviating from the operating point at 79.5 keV results in an increase in interaction efficiency.

To demonstrate that this behavior arises from variations in the resonance position, Fig. 6 shows the axial positions z at which the resonance condition is satisfied for the case without beam spreads. As expected, the resonance position generally shifts to

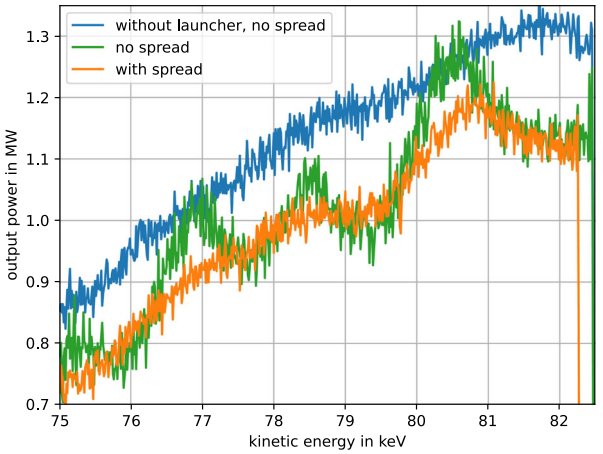

Fig. 5 EU ITER gyrotron output power as a function of the electron beam energy. The simulations are performed without spread (green), with spread (orange), and without ACI and spread (blue)

larger z with increasing E_{kin}, as γ_0/γ correspondingly increases. However, due to the variation in $\beta_z(z)$, the resulting curve exhibits a waveform-like modulation.

This approach appears promising, but it is difficult to be directly linked to experimental data, as some parameters are unknown under real conditions, so further more consistent improvements will be explored.

3.2 Impact of Launcher Radius

To investigate the effect of launcher geometry on ACI, similar simulations were performed for increased launcher oversize factors of 1.1, 1.2, 1.3, and 1.5, using the same

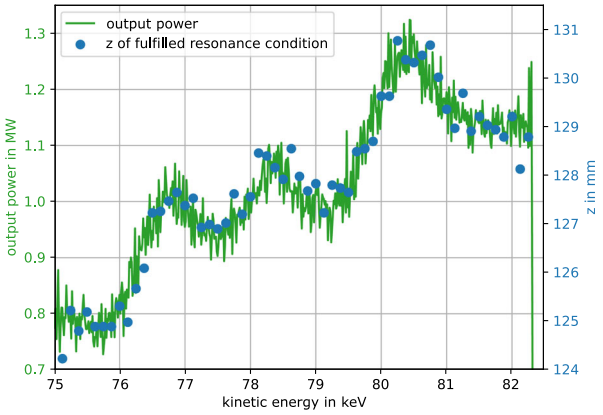

Fig. 6 Gyrotron output power as a function of electron kinetic energy, with the overlaid positions along z where the resonance condition is satisfied (blue markers)

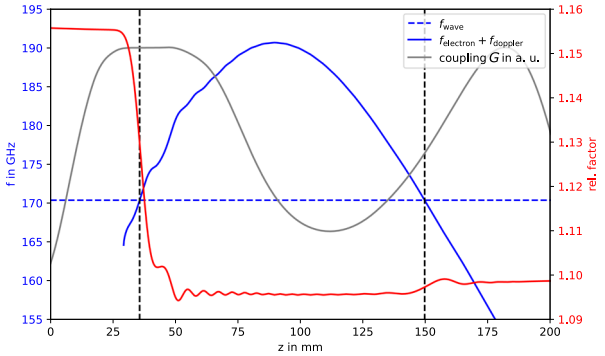

Fig. 7 Change of $f(z)$ (blue), $\gamma(z)$ (red), and $G(z)$ (gray) for a launcher with an oversize factor of 1.2

operating point as specified in Table 1 and analogous to the simulations shown in Figs. 5 and 3.

For example, increasing the oversize factor to 1.2, as illustrated in Fig. 7, shifts the resonance condition for ACI to the larger axial position of $z = 149\,\text{mm}$, due to the increased Doppler term. The maximum of $G(z)$ moves even further, thereby reducing the effective strength of ACI. This reduction is reflected in the relativistic factor, which exhibits only minor variations around that point. The output power changes by 20 kW, and the interaction efficiency increases to 36.6 %.

An analysis of the electron spectra in Fig. 8a indicates that, for a launcher oversize factor of 1.2, the effect on the slowest electrons is also notably reduced. Their kinetic energy decreases by only about 2.9 keV, which correspondingly improves the collector efficiency.

For an oversize factor of 1.3, the low coupling coefficient primarily introduces an increased spread in the electron kinetic energy, while the average relativistic factor remains nearly unchanged. This energy spread still leads to partial deceleration of the slowest electrons, thereby reducing collector efficiency. At even larger launcher sizes, such as an oversize factor of 1.5, ACI is effectively completely suppressed.

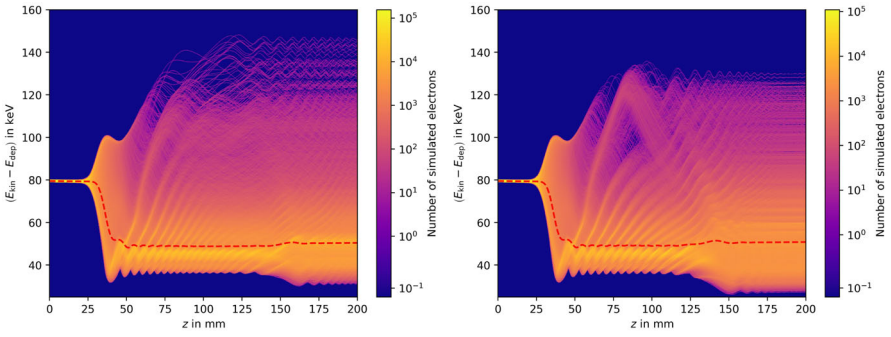

(a) oversize factor 1.2 (b) oversize factor 1.1

Fig. 8 Simulated electron distributions as a function of kinetic energy and axial position z with launchers of different oversize factors. The red dashed line shows the average kinetic energy

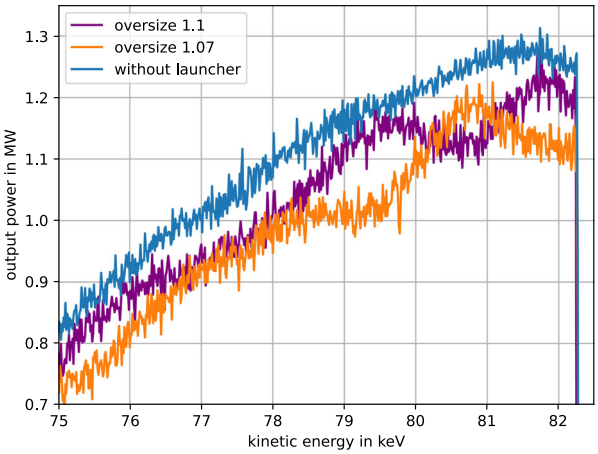

Fig. 9 Output power as a function of the electron beam energy including spreads. Purple and orange curves show simulations with different oversize factors for the launcher, while the blue curve represents a simulation without ACI, as the simulation is done only until the beginning of the launcher

While larger launchers are generally more effective in mitigating ACI, making them excessively oversized is impractical, as this would reduce the Gaussian mode content of the output beam at a given launcher length. Preserving the Gaussian content would require a substantial increase in launcher length, which is not feasible because the electron beam expands considerably as the magnetic field decreases, potentially leading to interception at the launcher walls. Nevertheless, a moderate adjustment of the launcher size appears feasible when employing a hybrid-type launcher [16]. Increasing the oversize factor to 1.1 already yields an interaction efficiency of 36.3 % and increases the kinetic energy of the lowest 5 % of electrons to 31.2 keV.

As previously noted, achieving this exact operating point experimentally cannot be guaranteed. Therefore, Fig. 9 presents the results for different kinetic energies. In most cases, the performance surpasses that obtained with an oversize factor of 1.07, and even under the least favorable conditions, it remains superior to the corresponding 1.07 case.

3.3 Influence of the Magnetic Field Profile

Besides $\beta_z(z)$, the guiding center radius, and therefore the magnetic field profile, has a major contribution to the amount of energy reconverted by ACI. Following ACI can be modified by modifying the shape of $B(z)$. For a consistent comparison, an arbitrary magnetic field profile is introduced after $z = 80\,\text{mm}$, leaving the main interaction unaffected. The corresponding magnetic field profiles are shown in Fig. 1.

The resulting dependencies of $f(z)$, $G(z)$, and $\gamma(z)$ for a steeper and a flatter magnetic field are plotted in Fig. 10, else using the same parameters as in Fig. 2. As expected, the position of ACI shifts in accordance with the magnetic field profile, while remaining close to the location of maximum coupling.

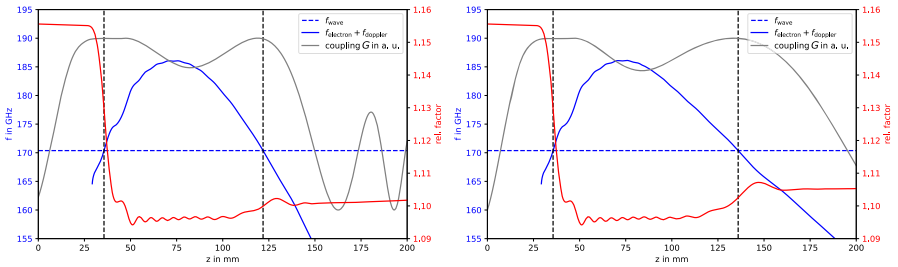

(a) steep magnetic field (b) flat magnetic field

Fig. 10 Change of $f(z)$ (blue), $\gamma(z)$ (red), and $G(z)$ (gray) for different magnetic field profiles

The behavior of $\gamma(z)$ indicates that the amplitude of ACI decreases with increasing magnetic field gradient. A steeper gradient shortens the spatial region over which the resonance condition Eq. 6 is satisfied, thereby limiting the overall interaction strength. Consequently, the interaction efficiency increases to 35.3 % for the steeper magnetic field, compared to the 32.9 % for the flatter profile.

Although a steeper magnetic field is always beneficial for reducing ACI, regardless of the operating point, it entails practical challenges. Implementing a steeper field would require a modified magnet design, which is both technologically demanding and costly. An alternative approach could involve shifting the magnetic field profile toward smaller axial positions, causing the resonance condition to occur in a steeper region and thereby reducing the effective range of ACI. However, this adjustment also steepens the field within the cavity, leading to efficiency losses or potentially the excitation of parasitic modes. For these reasons, such solutions are not considered further in this work.

For a larger oversized launcher, as discussed in Sect. 3.2, the magnetic field profile corresponding to the fulfilled resonance condition is lower and therefore exhibits a steeper gradient. This represents an additional advantage of using a larger launcher.

4 Conclusion and Outlook

In this work, three approaches to mitigate the effects of ACI in gyrotrons have been analyzed. Adjusting the operating point is the simplest method, as it generally requires no hardware modifications. However, in practice, this approach is challenging because key parameters, such as the pitch factor α, are not precisely known during operation. Moreover, changing the operating point can affect the cavity interaction, potentially leading to a net loss in efficiency despite a reduction in ACI. Consequently, the expected improvement from this strategy is limited.

A more effective approach involves introducing a steep magnetic field gradient in the launcher region, which significantly reduces the spatial range over which ACI can occur. Nevertheless, redesigning and constructing a new magnet system is technically complex and financially demanding. While impractical for existing systems, consideration of ACI in the magnet design could benefit future gyrotron developments.

From a practical standpoint, increasing the launcher radius size provides the most balanced solution. Although highly oversized launchers are not realistic, moderate oversizing can yield already measurable benefits. For example, an oversize factor of 1.1 enhances the interaction efficiency of the EU ITER gyrotron already by approximately 3.9 %.

Acknowledgements This work has been carried out within the framework of the EUROfusion Consortium, funded by the European Union via the Euratom Research and Training Programme (Grant Agreement No 101052200—EUROfusion). Views and opinions expressed are, however, those of the author(s) only and do not necessarily reflect those of the European Union or the European Commission. Neither the European Union nor the European Commission can be held responsible for them.
The authors acknowledge support by the state of Baden-Württemberg through bwHPC.
The authors gratefully acknowledge the computing time provided on the high-performance computer HoreKa by the National High-Performance Computing Center at KIT (NHR@KIT). This center is jointly supported by the Federal Ministry of Education and Research and the Ministry of Science, Research and the Arts of Baden-Württemberg, as part of the National High-Performance Computing (NHR) joint funding program (https://www.nhr-verein.de/en/our-partners). HoreKa is partly funded by the German Research Foundation (DFG).

Author Contributions A.S. drafted the manuscript and acquired and analyzed the data. C.W. developed and provided the software used in this work. M.T. and K.A. provided relevant archival materials and prior literature. S.I., J.J., L.F., and M.T. contributed to the conceptual development of the study and the interpretation of the data. All authors reviewed the manuscript.

Funding Open Access funding enabled and organized by Projekt DEAL. This work has been funded by the European Union via the Euratom Research and Training Programme (Grant Agreement No 101052200—EUROfusion).

Data Availability No datasets were generated or analysed during the current study.

Declarations

Ethics Approval and Consent to Participate Not applicable.

Competing Interests The authors declare no competing interests.

References

1. Zapevalov, V.E., Moiseev, M.A.: Influence of Aftercavity Interaction on Gyrotron Efficiency. Radiophysics and Quantum Electronics **47**(7), 520–527 (2004). https://doi.org/10.1023/B:RAQE.0000047243.18212.1d
2. Sinitsyn, O.V., Nusinovich, G.S.: Analysis of aftercavity interaction in gyrotrons. Physics of Plasmas **16**(2), 023101 (2009). https://doi.org/10.1063/1.3072978

3. Sinitsyn, O.V., Nusinovich, G.S., Antonsen, T.M.: Possibilities for reducing the aftercavity interaction effect in gyrotrons. Physics of Plasmas **17**(8), 083106 (2010). https://doi.org/10.1063/1.3469577
4. Kern, S., Avramides, K.A., Choudhury, A.R., Dumbrajs, O., Gantenbein, G., Illy, S., Samartsev, A., Schlaich, A., Thumm, M.: Simulation and experimental investigations on dynamic after cavity interaction (ACI). 35th International Conference on Infrared, Millimeter, and Terahertz Waves, 1–2 (2010). https://doi.org/10.1109/ICIMW.2010.5612609
5. Avramidis, K.A., Ioannidis, Z.C., Kern, S., Samartsev, A., Pagonakis, I.G., Tigelis, I.G., Jelonnek, J.: A comparative study on the modeling of dynamic after-cavity interaction in gyrotrons. Physics of Plasmas **22**(5), 053106 (2015). https://doi.org/10.1063/1.4919924
6. Roy Choudhury, A., Kern, S., Thumm, M.: Study of Dynamic After Cavity Interaction in Gyrotrons—Part I: Adiabatic Approximation. IEEE Transactions on Electron Devices **62**(1), 184–191 (2015). https://doi.org/10.1109/TED.2014.2368631
7. Roy Choudhury, A., D'Andrea, D., Thumm, M.: Study of Dynamic After Cavity Interaction in Gyrotrons—Part II: Influence of a Nonuniform Magnetic Field. IEEE Transactions on Electron Devices **62**(1), 192–199 (2015). https://doi.org/10.1109/TED.2014.2367314
8. Brand, G.F.: Mode conversion in a Gyrotron at a waveguide-taper junction. International Journal of Infrared and Millimeter Waves **5**(6), 839–851 (1984). https://doi.org/10.1007/BF01010205
9. Avramidis, K.A., Marek, A., Chelis, I., Ioannidis, Z.C., Feuerstein, L., Jelonnek, J., Thumm, M., Tigelis, I.: Simulation of Parasitic Backward-Wave Excitation in High-Power Gyrotron Cavities. IEEE Transactions on Electron Devices **70**(4), 1898–1905 (2023). https://doi.org/10.1109/TED.2023.3242216
10. Avramidis, K.A., Ioannidis, Z.C., Illy, S., Jin, J., Ruess, T., Aiello, G., Thumm, M., Jelonnek, J.: Multifaceted Simulations Reproducing Experimental Results From the 1.5-MW 140-GHz Preprototype Gyrotron for W7-X. IEEE Transactions on Electron Devices **68**(6), 3063–3069 (2021). https://doi.org/10.1109/TED.2021.3075653
11. Genoud, J., Alberti, S., Hogge, J.-P., Avramidis, K., Braunmüller, F., Bruschi, A., Bin, W., Dubray, J., Fasel, D., Gantenbein, G., Garavaglia, S., Goodman, T., Illy, S., Jin, J., Legrand, F., Marchesin, R., Pagonakis, I., Siravo, U., Toussaint, M.: Experimental characterization of the TCV dual-frequency gyrotron and validation of numerical codes including the effect of After Cavity Interaction. EPJ Web of Conferences **313**, 04008 (2024). https://doi.org/10.1051/epjconf/202431304008
12. Ioannidis, Z.C., Rzesnicki, T., Albajar, F., Alberti, S., Avramidis, K.A., Bin, W., Bonicelli, T., Bruschi, A., Chelis, I., Frigot, P.-E., Gantenbein, G., Hermann, V., Hogge, J.-P., Illy, S., Jin, J., Jelonnek, J., Kasparek, W., Latsas, G., Lechte, C., Legrand, F., Kobarg, T., Pagonakis, I.G., Rozier, Y., Schlatter, C., Schmid, M., Tigelis, I.G., Thumm, M., Tran, M.Q., Zein, A., Zisis, A.: CW Experiments With the EU 1-MW, 170-GHz Industrial Prototype Gyrotron for ITER at KIT. IEEE Transactions on Electron Devices **64**(9), 3885–3892 (2017). https://doi.org/10.1109/TED.2017.2730242
13. Kartikeyan, M.V., Borie, E., Thumm, M.K.A.: Gyrotrons: High-power Microwave and Millimeter Wave Technology. Advanced texts in physics. Springer, Berlin, Germany (2004). https://doi.org/10.1007/978-3-662-07637-8. ISBN: 978-3-540-40200-8
14. Wu, C., Feuerstein, L., Schmidt, A., Illy, S., Thumm, M., Jelonnek, J.: ROCK: A Flexible Gyrotron Cavity Simulation Toolkit Using an Accuracy-Improved Time-Dependent Self-Consistent Multimode Interaction Model. Journal of Infrared, Millimeter, and Terahertz Waves **46**(7), 50 (2025). https://doi.org/10.1007/s10762-025-01065-5
15. Choi, E.M., Shapiro, M.A., Sirigiri, J.R., Temkin, R.J.: Experimental observation of the effect of aftercavity interaction in a depressed collector gyrotron oscillator. Physics of Plasmas **14**(9), 093302 (2007). https://doi.org/10.1063/1.2776911
16. Jin, J., Thumm, M., Gantenbein, G., Jelonnek, J.: A Numerical Synthesis Method for Hybrid-Type High-Power Gyrotron Launchers. IEEE Transactions on Microwave Theory and Techniques **65**(3), 699–706 (2017). https://doi.org/10.1109/TMTT.2016.2630060